


## Article

# Strong Magnetic p-n Heterojunction Fe<sub>3</sub>O<sub>4</sub>-FeWO<sub>4</sub> for Photo-Fenton Degradation of Tetracycline Hydrochloride

Binger Bai <sup>1,2</sup>, Guanrong Cheng <sup>3</sup>, Jian Chen <sup>1,\*</sup>, Xiaoping Chen <sup>4</sup>  and Qizhao Wang <sup>2,\*</sup>

<sup>1</sup> College of Chemistry and Materials Science, Huaibei Normal University, Huaibei 235000, China; bbehope@163.com

<sup>2</sup> School of Water and Environment, Chang'an University, Xi'an 710054, China

<sup>3</sup> Shaanxi Construction Engineering Fire Technology Service Center, Xi'an 710000, China; sxxffwzx@163.com

<sup>4</sup> Institute of Energy Research, Jiangxi Academy of Sciences, Nanchang 330096, China; cpxjxsky@126.com

\* Correspondence: chenjian@chnu.edu.cn (J.C.); qzwang@chd.edu.cn (Q.W.)

**Abstract:** With the abuse of antibiotics, its pollution poses an increasing threat to the environment and human health. Effective degradation of organic pollutants in water bodies is urgent. Compared to traditional treatment methods, advanced oxidation processes that have developed rapidly in recent years are more environmentally friendly, efficient and applicable to a wider range of organic compounds. FeWO<sub>4</sub> was used in this study as the iron-based semiconductor material to modify and optimize the material design. Fe<sub>3</sub>O<sub>4</sub>/FeWO<sub>4</sub> composites were prepared by a two-step hydrothermal method. The crystal structure, surface morphology, electrochemical properties and separability of the composite semiconductor were analyzed by XRD, XPS, UV-vis, SEM, EDS and Mott-Schottky. The results showed that, when the initial contaminant concentration was 30 mg/L, the initial solution pH was 4, the dosage of the catalyst was 25 mg and the dosage of hydrogen peroxide was 30 μL, the degradation efficiency of tetracycline hydrochloride (TCH) could reach 91% within 60 min, which was significantly improved compared to the performance of the single semiconductors Fe<sub>3</sub>O<sub>4</sub> and FeWO<sub>4</sub>. In addition, the catalyst prepared in this experiment can be easily recovered by magnetic separation technology in practical application, which will not affect the turbidity of water while reducing the cost of catalyst separation and recovery.

**Keywords:** photo-Fenton; FeWO<sub>4</sub>; composite material; magnetic separation; organic pollutants



**Citation:** Bai, B.; Cheng, G.; Chen, J.; Chen, X.; Wang, Q. Strong Magnetic p-n Heterojunction Fe<sub>3</sub>O<sub>4</sub>-FeWO<sub>4</sub> for Photo-Fenton Degradation of Tetracycline Hydrochloride. *Catalysts* **2024**, *14*, 453. <https://doi.org/10.3390/catal14070453>

Academic Editor: Enric Brillas

Received: 28 May 2024

Revised: 5 July 2024

Accepted: 10 July 2024

Published: 14 July 2024



**Copyright:** © 2024 by the authors. Licensee MDPI, Basel, Switzerland. This article is an open access article distributed under the terms and conditions of the Creative Commons Attribution (CC BY) license (<https://creativecommons.org/licenses/by/4.0/>).

## 1. Introduction

Antibiotics are recognized as key drugs that seriously harm the environment and human health. They enter natural water bodies through sewage treatment plants, aquaculture, livestock farming, improper drug disposal and other ways, posing a threat to the environment and human health [1–3]. Among them, tetracycline antibiotics are absorbed with difficulty by organisms, degrade the environment, and are difficult to completely remove from conventional sewage treatment systems, posing a serious threat to the ecosystem and human health [4,5]. Therefore, it is necessary to develop an economical and effective treatment method for tetracycline antibiotics.

Nowadays, there are various treatment methods, such as the physical method (adsorption, magnetic separation, etc.) [6–8], the chemical method (ozonation, coagulation, etc.) [9–11] and the biological method (biofilm, anaerobic biological treatment, etc.) [12,13], which are widely used for the treatment of antibiotics. In recent years, advanced oxidation technologies have also developed rapidly, which can produce active substances with strong oxidation, degrade refractory macromolecular organic matter in wastewater, and thus achieve efficient mineralization and effectively remove antibiotics [14–16]. Among them, the heterogeneous photo-Fenton method combines the advantages of photocatalysis and the Fenton method, which uses sunlight to carry out a photocatalytic reaction, making the treatment process green, pollution-free and releases a large amount energy [17,18]. At the

same time, hydrogen peroxide can be introduced to improve the yield of  $\cdot\text{OH}$  and form an iron cycle reaction, which reduces the consumption of ferrous ions ( $\text{Fe}^{2+}$ ) and avoids the production of iron sludge. It enhances the oxidative degradation effect of organic matter and improves the efficiency of treating organic polluted wastewater [19–22]. It not only reduces the operating cost, but also reduces the risk of secondary pollution, which is a very promising wastewater treatment technology.

$\text{FeWO}_4$ , also known as iron tungstate, is the main component of wolstenite with a band gap of about 2.0 eV and a wide photoresponse range. It is a P-type semiconductor photocatalyst that can form a good synergistic reaction with the Fenton reaction [23,24]. Under sunlight,  $\text{FeWO}_4$  effectively absorbs and uses light energy, triggering a photocatalytic reaction that breaks down organic pollutants in water. However, its photocatalytic performance is not satisfactory due to the rapid recombination of photogenerated electron hole pairs, so it is necessary to modify it to improve the photogenerated electron hole separation rate and delay the recombination time to improve the degradation ability. In order to explore ways to improve the degradation ability of  $\text{FeWO}_4$ , researchers have carried out a large number of studies to improve the electron hole separation efficiency of  $\text{FeWO}_4$  and slow down its recombination by doping metal and non-metal elements or introducing other semiconductor materials to form heterogeneous structures [25–27]. Wang et al. [28] prepared a  $g\text{-C}_3\text{N}_4/\text{FeWO}_4$  Z-type heterojunction photocatalyst through the hydrothermal method, and the tetracycline degradation rate reached almost 100% within 60 min under visible light irradiation with persulfate. The construction of Z-type heterojunction made the electrons on CB of  $\text{FeWO}_4$  move to VB of  $g\text{-C}_3\text{N}_4$ . Thus, the photogenerated electron hole pair recombination of  $\text{FeWO}_4$  was inhibited, and the holes left in VB of  $\text{FeWO}_4$  could react with  $\text{H}_2\text{O}$  to form  $\bullet\text{OH}$ , which greatly improves the degradation performance. As an N-type semiconductor,  $\text{Fe}_3\text{O}_4$  has good stability, and its narrow band gap can supplement the light absorption capacity of the catalyst with a wider wavelength range, so that the composite can make full use of sunlight and improve the efficiency of the photocatalytic reaction [29,30]. In addition,  $\text{Fe}_3\text{O}_4$  is magnetic and easy to recover, which facilitates separation, recovery and reuse of catalysts, thus improving economy and practicability [31–33]. Therefore, the combination of  $\text{FeWO}_4$  and  $\text{Fe}_3\text{O}_4$  is an effective strategy to slow down the recombination of photogenerated carriers and cause catalyst magnetic recovery, which has a certain research angle for the photofenton degradation of antibiotics.

In this study, a strong magnetic  $\text{Fe}_3\text{O}_4\text{-FeWO}_4$  p-n heterojunction catalyst composite was synthesized by a simple hydrothermal method, and tetracycline hydrochloride (TCH) was selected as the target pollutant for the photo-Fenton experiment to analyze its degradation performance. The morphology, structure and electrochemical properties of the materials were characterized by XRD, BET, SEM, XPS, FTIR and other techniques. The effects of pH, catalytic dose, TCH initial concentration and the addition of  $\text{H}_2\text{O}_2$  on the degradation performance were studied. In addition, the possible degradation mechanism was explored. The results showed that the presence of p-n heterojunction greatly increased the electron migration rate and delayed the recombination time of photogenerated electron holes. The  $\text{Fe(II)/Fe(III)}$  cycling rate in the heterogeneous photofenton process increased, and the degradation ability was improved. The stability and reusability of the composite were verified by magnetic recovery experiments.

## 2. Results and Discussion

### 2.1. Characterization

To confirm the morphology of the catalyst and the phase dispersion state of  $\text{Fe}_3\text{O}_4$  and  $\text{FeWO}_4$  in the composite material, SEM and EDS analyses were conducted on the synthesized materials. Firstly, Figure 1a shows the SEM image of  $\text{FeWO}_4$  nanomaterials, where their typical sheet-like structure can be observed. This structure provides a large specific surface area, which is beneficial for enhancing the activity of the photocatalyst [34–36]. Figure 1b presents the SEM image of  $\text{Fe}_3\text{O}_4$ , displaying its microsphere structure. These microspheres are densely packed together, resulting in a smaller exposed area, which might

be attributed to the magnetic properties of  $\text{Fe}_3\text{O}_4$  [37,38]. Figure 1c illustrates the SEM image of the 50%- $\text{Fe}_3\text{O}_4$ /FWO composite material. It can be seen that the  $\text{FeWO}_4$  sheet-like structure and  $\text{Fe}_3\text{O}_4$  microsphere structure are combined, with the microspheres attached to the sheet-like structure. This combination reduces the agglomeration phenomenon, indicating the successful compounding of the two materials. The combination likely increases the active sites for the photo-Fenton reaction and improves the adsorption capacity for pollutants. Further EDS analysis (Figure 1d–g) shows the distribution of elements in the composite material. The elements O, Fe and W are uniformly distributed in the composite. Figure 1h presents the EDS spectrum of the composite material, clearly showing the characteristic peaks of O, Fe and W, further confirming the presence of these elements. The weight percentage and atomic percentage analysis results indicate that the weight percentages of O, Fe and W in the composite are 18.4%, 47.6% and 34.0%, respectively, while the atomic percentages are 51.5%, 40.2% and 8.3%, respectively. These results further confirm the successful compounding of  $\text{Fe}_3\text{O}_4$  and  $\text{FeWO}_4$ , and the uniformity of the composite material.

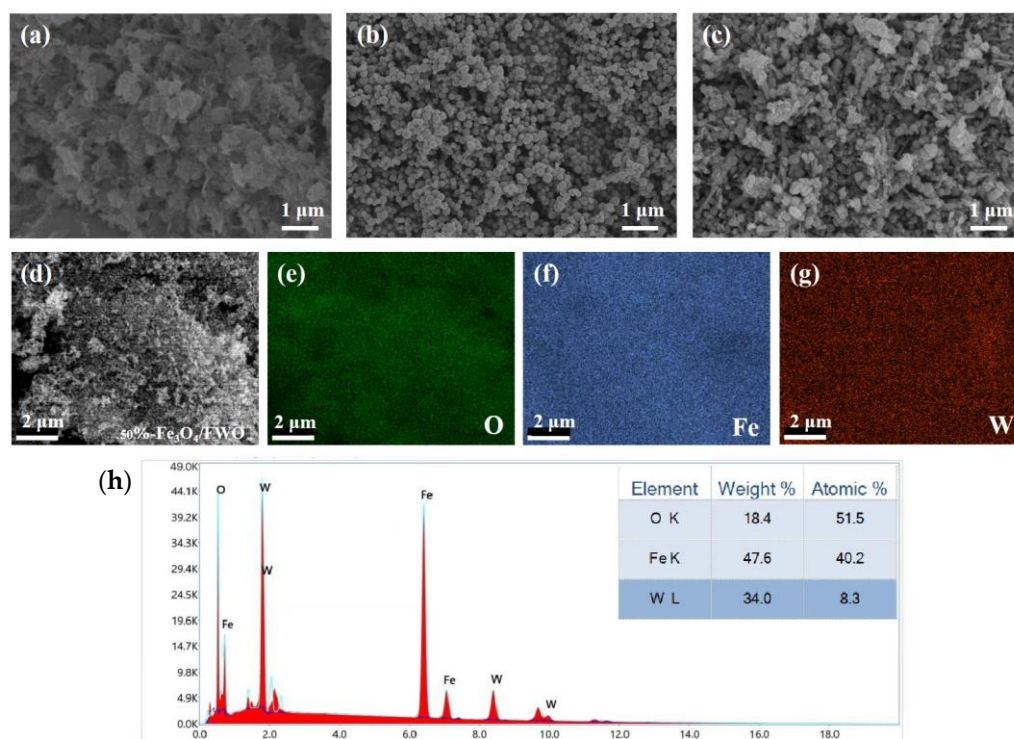


**Figure 1.** SEM images of (a)  $\text{FeWO}_4$ , (b)  $\text{Fe}_3\text{O}_4$  and (c) 50%- $\text{Fe}_3\text{O}_4$ /FWO; EDS image of 50%- $\text{Fe}_3\text{O}_4$ /FWO (d), mapping spectrum of (e) O, (f) Fe and (g) W; (h) EDAX of 50%- $\text{Fe}_3\text{O}_4$ /FWO.

Figure 2a shows the XRD patterns of the catalyst materials. The diffraction peaks of  $\text{Fe}_3\text{O}_4$  at  $30.2^\circ$ ,  $35.5^\circ$ ,  $43.2^\circ$ ,  $53.6^\circ$ ,  $57.1^\circ$ , and  $62.7^\circ$  correspond to the (220), (311), (400), (422), (511) and (440) crystal planes, respectively (JCPDS NO.88-0315) [39]. The diffraction peaks of  $\text{FeWO}_4$  at  $18.7^\circ$ ,  $23.8^\circ$ ,  $24.4^\circ$ ,  $30.4^\circ$ ,  $36.3^\circ$  and  $53.6^\circ$  are highly consistent with its standard card (JCPDS NO.74-1130), and the sharp and clear peaks indicate good crystallinity of the synthesized material [40]. In the  $\text{Fe}_3\text{O}_4$ /FWO composite material, the diffraction peaks of both  $\text{Fe}_3\text{O}_4$  and  $\text{FeWO}_4$  can be observed. As the  $\text{Fe}_3\text{O}_4$  content increases, the intensity of the peaks corresponding to  $\text{Fe}_3\text{O}_4$  increases, while the intensity of the peaks corresponding to  $\text{FeWO}_4$  decreases, indicating the successful preparation of x- $\text{Fe}_3\text{O}_4$ /FWO photocatalysts with different ratios. No other characteristic peaks are detected in the composite material, indicating no incorporation of other impurities.

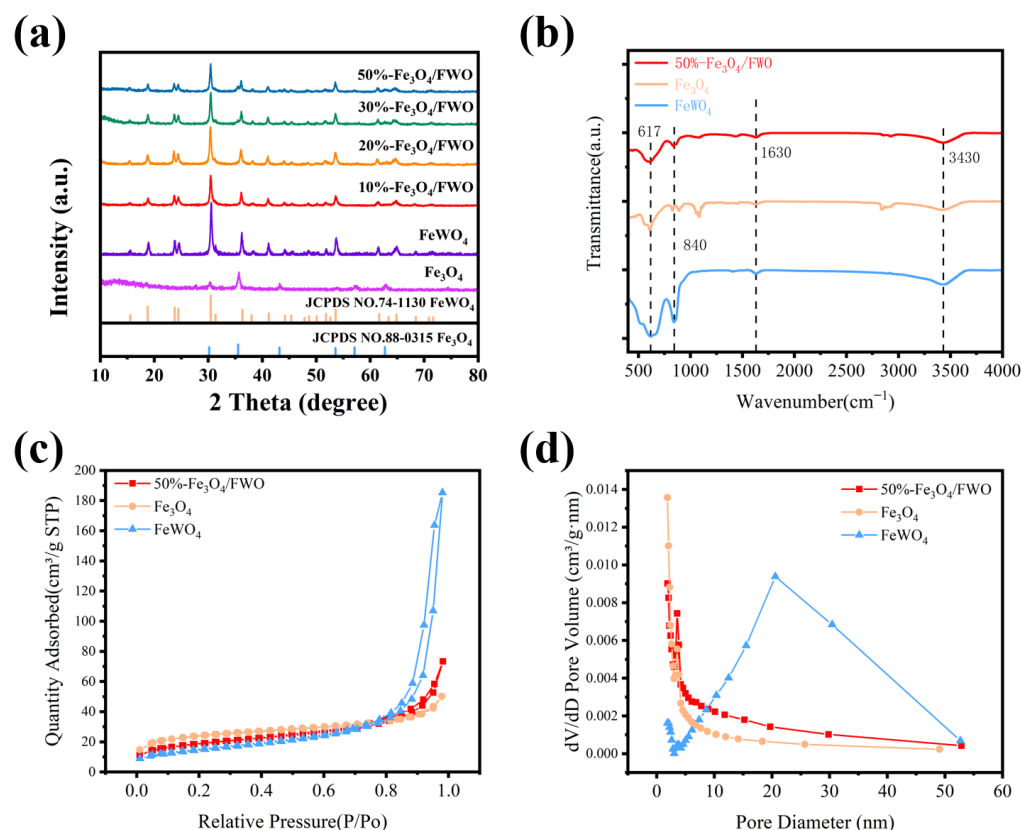


**Figure 2.** (a) XRD pattern image, (b) FT-IR diagram, (c) Nitrogen adsorption–desorption curves and (d) pore size distribution curves of  $\text{FeWO}_4$ ,  $\text{Fe}_3\text{O}_4$  and  $\text{Fe}_3\text{O}_4/\text{FWO}$ .

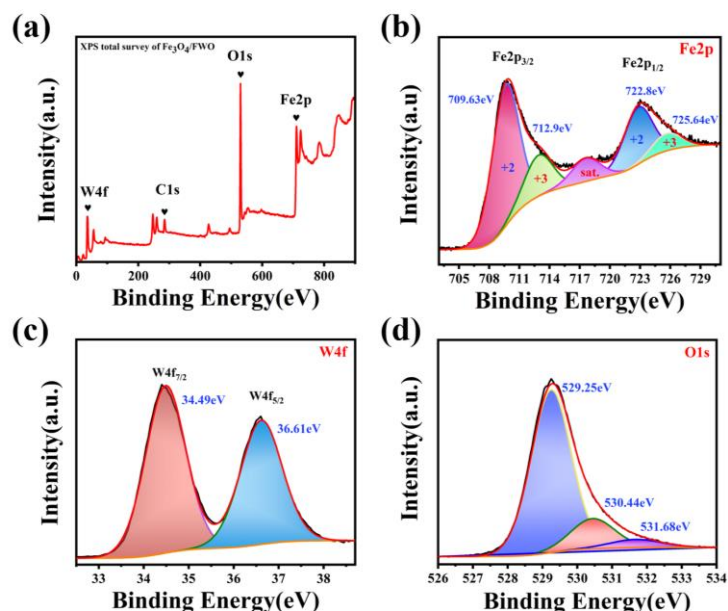
Figure 2b shows the FT-IR spectra of the prepared materials. The characteristic peak of  $\text{FeWO}_4$  at  $840\text{ cm}^{-1}$  corresponds to the W-O stretching vibration [41], and the characteristic peak of  $\text{Fe}_3\text{O}_4$  at  $617\text{ cm}^{-1}$  corresponds to the Fe-O stretching vibration [42]. In the FT-IR spectrum of the 50%- $\text{Fe}_3\text{O}_4/\text{FWO}$  composite material, both of these characteristic peaks are clearly visible, further proving the successful combination of  $\text{FeWO}_4$  and  $\text{Fe}_3\text{O}_4$ . Additionally, the broad peak centered at  $3430\text{ cm}^{-1}$  in the composite material is related to the O-H longitudinal stretching vibration of adsorbed water molecules [43].

Figure 2c displays the nitrogen adsorption–desorption isotherms of  $\text{FeWO}_4$ ,  $\text{Fe}_3\text{O}_4$  and 50%- $\text{Fe}_3\text{O}_4/\text{FWO}$ . The isotherms of these materials are of the typical type IV with obvious H3 hysteresis loops [44]. The analysis of specific surface area and pore volume indicates that  $\text{FeWO}_4$  has a specific surface area of  $53.1\text{ m}^2/\text{g}$  and a pore volume of  $0.002\text{ cm}^3/\text{g}$ , while  $\text{Fe}_3\text{O}_4$  possesses a specific surface area of  $86.7\text{ m}^2/\text{g}$  and a pore volume of  $0.029\text{ cm}^3/\text{g}$ . The 50%- $\text{Fe}_3\text{O}_4/\text{FWO}$  composite material exhibits a specific surface area of  $67.5\text{ m}^2/\text{g}$  and a pore volume of  $0.014\text{ cm}^3/\text{g}$ . Compared to pure  $\text{FeWO}_4$ , the incorporation of  $\text{Fe}_3\text{O}_4$  significantly enhances the specific surface area and pore volume of the composite, thereby providing more active sites and facilitating the diffusion and mass transfer of reactants [45]. The pore size distribution curves (Figure 2d) show that the average pore size of  $\text{FeWO}_4$  is 21.6 nm,  $\text{Fe}_3\text{O}_4$  is 3.6 nm and the 50%- $\text{Fe}_3\text{O}_4/\text{FWO}$  composite material has an average pore size of 6.7 nm, which lies between  $\text{FeWO}_4$  and  $\text{Fe}_3\text{O}_4$ . This further indicates the presence of mesoporous structures in these materials. The pore size distribution of the composite material is more concentrated compared to  $\text{FeWO}_4$ , which is more favorable for the adsorption and enrichment of TCH, thereby enhancing the efficiency of photocatalytic Fenton degradation [46].

Figure 3 presents the XPS survey and high-resolution spectra of 50%- $\text{Fe}_3\text{O}_4/\text{FWO}$ . Figure 3a indicates that the surface of the composite sample contains four elements: W 4f, Fe 2p, O 1s and C 1s. The survey spectrum shows that no other impurities are present in the sample, and the binding energies of the elements match their respective values. Figure 3b



shows the high-resolution spectrum of Fe 2p, where the peaks at 709.63 eV and 722.8 eV can be attributed to Fe 2p<sub>3/2</sub> and Fe 2p<sub>1/2</sub> of Fe<sup>2+</sup>, and the peaks at 712.9 eV and 725.64 eV can be attributed to Fe 2p<sub>3/2</sub> and Fe 2p<sub>1/2</sub> of Fe<sup>3+</sup>, and a satellite peak is observed at 717.6 eV [47]. Figure 3c displays the characteristic spectrum of W, with binding energies at 34.49 eV and 36.61 eV, corresponding to W 4f<sub>7/2</sub> and W 4f<sub>5/2</sub>, respectively [48]. Figure 3d shows the O 1s characteristic peaks at 529.25 eV, 530.44 eV and 531.68 eV [49]. The data obtained from XPS confirm the formation of the composite material.



**Figure 3.** XPS spectra of the 50%-Fe<sub>3</sub>O<sub>4</sub>/FWO composite: (a) survey, (b) Fe 2p, (c) W 4f and (d) O 1s.

The photocurrent response of the catalyst was analyzed by a photoelectric chemical test. It can be seen from Figure 4a that the photocurrent intensity of 50%-Fe<sub>3</sub>O<sub>4</sub>/FWO is significantly higher than that of pure Fe<sub>3</sub>O<sub>4</sub> and pure FeWO<sub>4</sub>. The higher the photocurrent intensity, the greater the photoinduced carrier separation ability [50], indicating that the formation of the heterointerface of Fe<sub>3</sub>O<sub>4</sub> and FeWO<sub>4</sub> is conducive to the separation of photoinduced electrons and holes, and can effectively prolong the recombination time of electron holes. In addition, according to the electrochemical impedance diagram of Figure 4b, 50%-Fe<sub>3</sub>O<sub>4</sub>/FWO has the smallest Nyquist arc radius, meaning the smallest charge transfer resistance, which is the result of the rapid transfer of photogenerated carriers [51].

The light response ability of the material was tested by UV-vis. The two pure samples in Figure 4c both showed excellent visible light response ability, indicating that Fe<sub>3</sub>O<sub>4</sub> and FeWO<sub>4</sub> had a very significant absorption ability of sunlight, and the composite material still had a strong response ability. This facilitates the absorption of sunlight and the creation of electron holes [52]. After analyzing and calculating the absorbance of the obtained material, Figure 4d was obtained. As shown in the figure, the band-gap width of FeWO<sub>4</sub> was  $E_g = 2.5$  eV, and that of Fe<sub>3</sub>O<sub>4</sub> was  $E_g = 2.2$  eV.

In order to determine the semiconductor type and band-gap position of the catalyst, the Mott-Schottky test was performed on FeWO<sub>4</sub> and Fe<sub>3</sub>O<sub>4</sub> catalysts, respectively. We took the longest straight line part of the curve in the figure as a tangent to distinguish the type of semiconductor. The tangent slope of Figure 4e was negative, indicating that FeWO<sub>4</sub> is a p-type semiconductor, and the tangent slope of Figure 4f was positive, so Fe<sub>3</sub>O<sub>4</sub> is an n-type semiconductor [53]. In addition, the conduction band position and valence band position of the semiconductor can be obtained from the intersection position of the tangent and the X-axis in the figure. The intersection position of the p-type semiconductor is the valence band position, and the intersection position of the n-type semiconductor is the

conduction band position. Therefore, the valence band of  $\text{FeWO}_4$  is  $E_{\text{VB}} = 2.2 \text{ eV}$ , and the conduction band of  $\text{Fe}_3\text{O}_4$  is  $E_{\text{CB}} = -0.7 \text{ eV}$ .

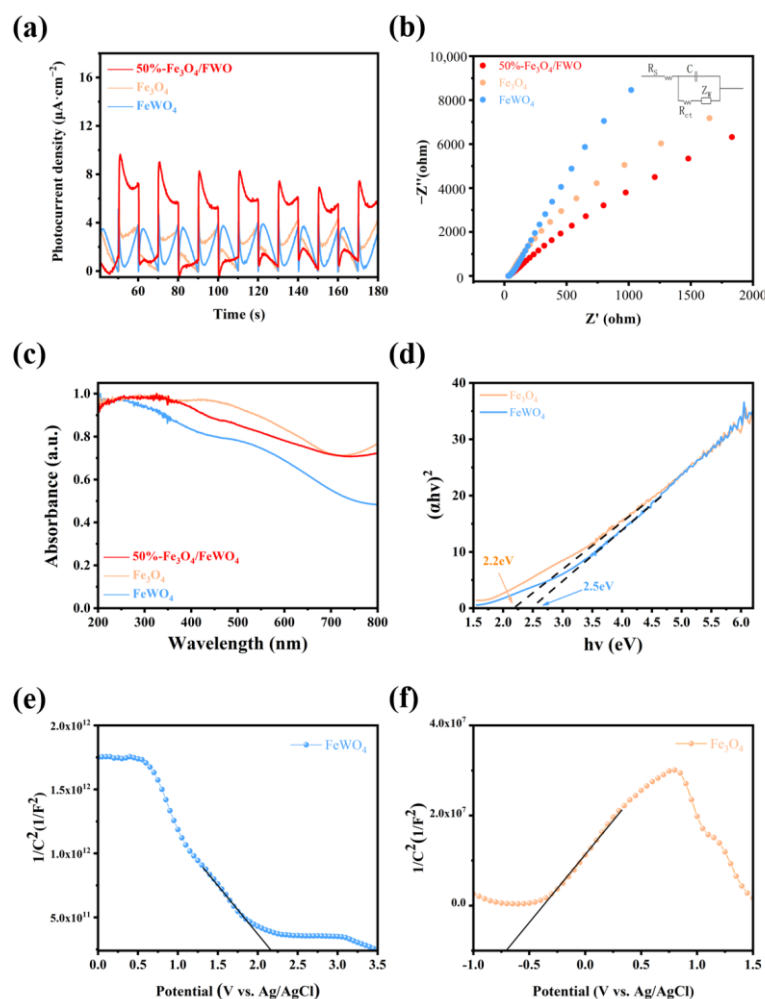


**Figure 4.** (a) It curves and (b) EIS curves of catalysts; (c) The UV-vis absorption spectra of  $\text{FeWO}_4$ ,  $\text{Fe}_3\text{O}_4$  and 50%- $\text{Fe}_3\text{O}_4/\text{FWO}$ ; (d) The band gap of semiconductor; Mott-Schottky chart of (e)  $\text{FeWO}_4$  and (f)  $\text{Fe}_3\text{O}_4$ .

## 2.2. Photo-Fenton Reaction Performance

The photo-Fenton degradation performance of the catalyst was evaluated by using TCH as the target pollutant under visible light irradiation. The reaction conditions were as follows: the concentration of TCH was 20 mg/L, the solution volume was 40 mL,  $\text{H}_2\text{O}_2$  dosage was 20  $\mu\text{L}$ , catalyst dosage was 25 mg, pH was not adjusted and temperature was room temperature. Figure 5a shows the degradation performance of tetracycline hydrochloride by catalysts of different composite proportions. It can be seen from the figure that the adsorption–desorption equilibrium is reached after dark adsorption for 30 min, and the adsorption capacity of catalysts of different proportions is different. Until the proportion of  $\text{Fe}_3\text{O}_4$  increased to 50% to reach the critical point, and when the proportion of  $\text{Fe}_3\text{O}_4$  increased to 70%, its adsorption capacity and degradation capacity decreased. In order to compare the degradation rates at different ratios, the first-order reaction kinetics were fitted to the sample degradation data. As shown in Figure 5b, the first-order reaction kinetics constant of 50%- $\text{Fe}_3\text{O}_4/\text{FWO}$  was the highest, and the corresponding reaction degradation rate was the highest. Therefore, among the catalysts of various proportions, 50%- $\text{Fe}_3\text{O}_4/\text{FWO}$  had the best catalytic degradation performance.

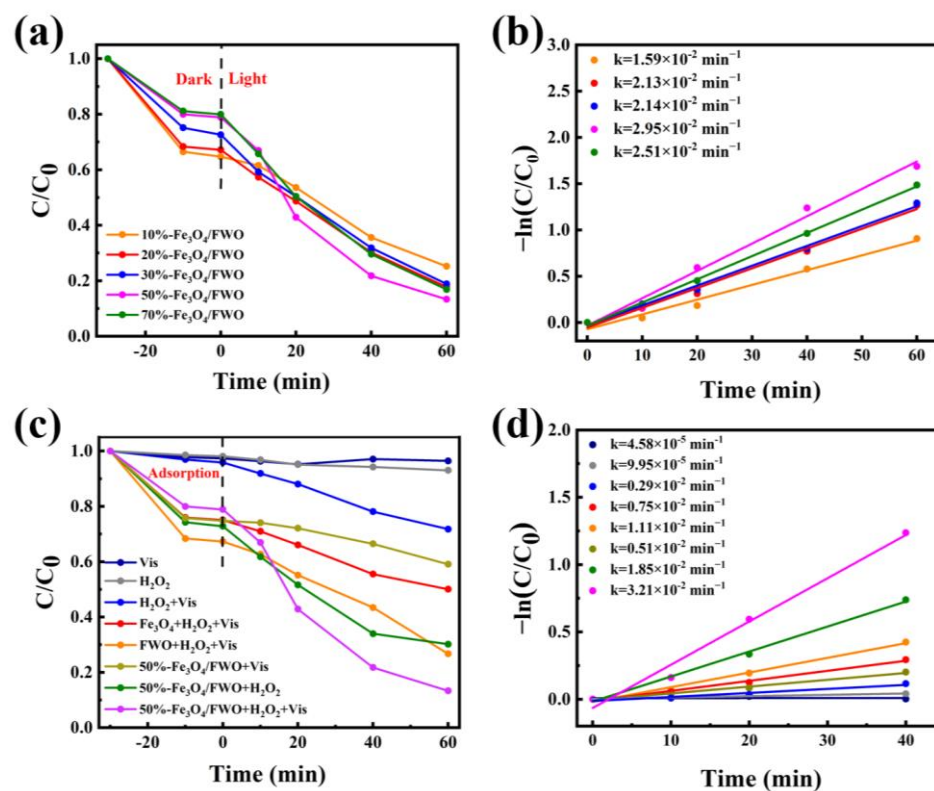


**Figure 5.** (a) Different ratios of  $\text{Fe}_3\text{O}_4/\text{FWO}$  and (b) degradation kinetics, (c) TCH degradation efficiency of different systems and (d) degradation kinetics.

In order to further study the effects of visible light and  $\text{H}_2\text{O}_2$  on degradation, as well as the improvement of the performance of composite materials compared with a single semiconductor, degradation analysis of different systems was carried out under the same reaction conditions, and the results are shown in Figure 5c,d. As can be seen from Figure 5c, the degradation effect of TCH is not obvious under the conditions of visible light,  $\text{H}_2\text{O}_2$ , or both. When 50%- $\text{Fe}_3\text{O}_4/\text{FWO}$  composite catalyst was added, the degradation effect changed significantly, and the degradation efficiency reached 41% under photocatalysis and 70% under the Fenton condition. The solution efficiency reached 87% under the photo-Fenton condition, which is significantly improved compared to  $\text{FeWO}_4$  (74%) or  $\text{Fe}_3\text{O}_4$  (50%) alone. It can be seen that there was a synergistic effect between visible light and the Fenton reaction, and their combined action can significantly improve catalytic degradation efficiency. At the same time, the heterojunction formed by  $\text{Fe}_3\text{O}_4$  and  $\text{FeWO}_4$  can improve the transfer efficiency of photogenerated electron holes, delay the recombination of electron holes and improve the photo-Fenton performance. Figure 5d is the fitting curve of the first-order reaction kinetics of different reaction systems. As shown in the figure, the first-order reaction kinetic constant of 50%- $\text{Fe}_3\text{O}_4/\text{FWO}$  under the photo-Fenton condition is  $3.21 \times 10^{-2} \text{ min}^{-1}$ , which corresponds to the highest kinetic constant of degradation efficiency. It is three times and four times that of  $\text{FeWO}_4$  and  $\text{Fe}_3\text{O}_4$ , respectively. Therefore, the combination of  $\text{Fe}_3\text{O}_4$  and  $\text{FeWO}_4$  can significantly improve the photo-Fenton degradation ability.

### 2.3. Different Influencing Factors

Figure 6a shows the degradation curves of TCH at different initial pH conditions (Catalyst = 25 mg,  $\text{H}_2\text{O}_2$  = 30  $\mu\text{L}$ , TCH = 20 mg/L, 40 mL). It can be seen that the catalyst has a high degradation ability at different pH values, indicating that the composite catalyst has a wide pH adaptation range. In practical applications, it can be well adapted to a variety of weak acidic and weak alkaline wastewater. In addition, when pH = 4, the degradation efficiency could reach 91% within 60 min, so pH = 4 was used in the subsequent experiment.

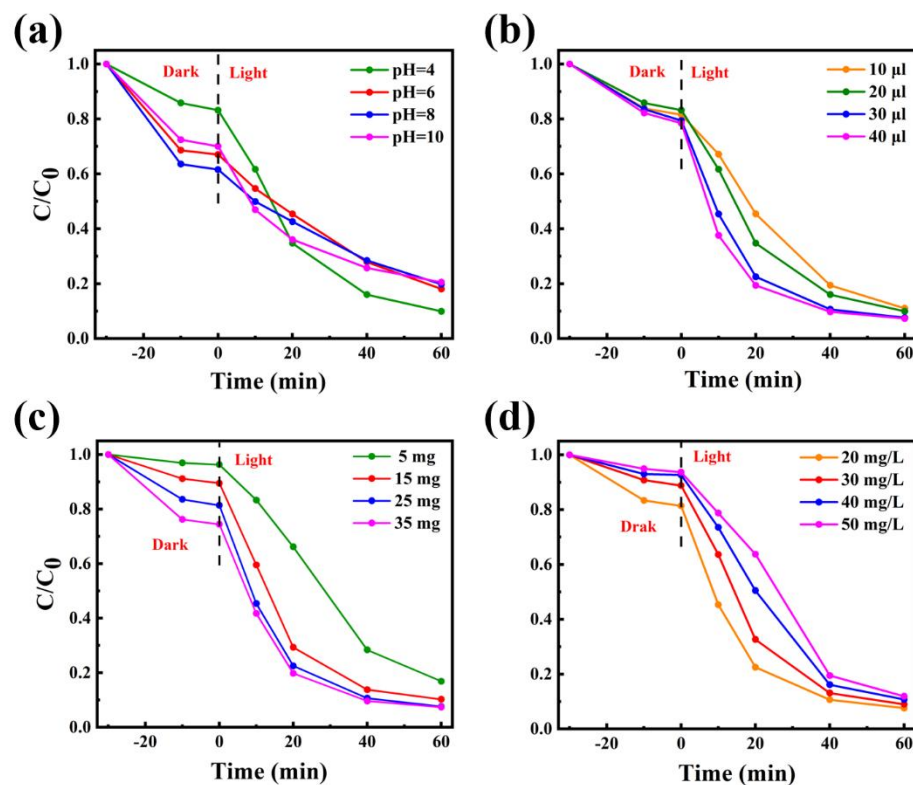


**Figure 6.** Effects of (a) pH, (b) the amount of  $\text{H}_2\text{O}_2$ , (c) catalyst dosage and (d) initial TCH concentration on degradation performance.

Figure 6b shows the degradation curves of different  $\text{H}_2\text{O}_2$  supplemental levels (Catalyst = 25 mg, TCH = 20 mg/L, 40mL, pH = 4). In this figure, the addition of  $\text{H}_2\text{O}_2$  gradually increased from 10  $\mu\text{L}$  to 40  $\mu\text{L}$ , and although the final degradation efficiency is similar, it can be seen from the figure that there was a significant difference in degradation rate when the addition of hydrogen peroxide increased from 10  $\mu\text{L}$  to 30  $\mu\text{L}$ , while the effect from the addition of 40  $\mu\text{L}$  was almost the same as from the addition of 30  $\mu\text{L}$ . Therefore, considering economy and practicability, the amount of hydrogen peroxide added was not increased, and 30  $\mu\text{L}$  was selected as the addition amount for subsequent experiments.

Figure 6c shows the degradation process of TCH by photo-Fenton using a catalyst as a variable ( $\text{H}_2\text{O}_2$  = 30  $\mu\text{L}$ , TCH = 20 mg/L, 40mL, pH = 4). The amount of catalyst increased from 5 mg to 35 mg, and it can be seen from the figure that there was no significant change after the degradation efficiency increased to a certain extent. On the one hand, this may be due to the excessive addition of the catalyst, which affects the absorption of visible light and reduces the generation of photogenerated electron holes, thus slowing down the degradation rate. On the other hand, the catalytic reaction rate has a limit value and cannot be raised indefinitely. Since the effect of 25 mg versus 35 mg is not very different, 25 mg was selected as the dosage of catalyst in the subsequent experiment.

Finally, the initial concentration of pollutants was studied experimentally (Catalyst = 25 mg,  $\text{H}_2\text{O}_2$  = 30  $\mu\text{L}$ , TCH = 40mL, pH = 4). In Figure 6d, the concentration of tetracycline hydrochloride increased from 20 mg/L to 50 mg/L, and it can be seen that the 50%- $\text{Fe}_3\text{O}_4$ /FWO composite catalyst had a strong degradation ability for TCH, and the degradation efficiency was 93% when the concentration was 20 mg/L. Even if the concentration is increased to 50 mg/L, the degradation efficiency of 89% can be achieved within 60 min. During pollutant degradation, high concentrations of pollutants may block or consume  $\text{H}_2\text{O}_2$  by depleting reactive oxygen species, adsorbing and obstructing the photocatalyst surface and triggering by-product side reactions. This reduces the efficiency of  $\text{H}_2\text{O}_2$  utilization, thereby lowering the degradation efficiency [54]. Considering that the



degradation efficiency is basically the same when the pollutant concentration is 20 mg/L and 30 mg/L, 30 mg/L was chosen as the final initial pollutant concentration.

Through the investigation of single-factor effects, the optimal experimental conditions were determined. Under visible light, with an initial pollutant concentration of 30 mg/L, an initial solution pH of 4, a catalyst dosage of 25 mg and an addition of 30  $\mu$ L of hydrogen peroxide, the degradation efficiency of tetracycline hydrochloride by the 50%-Fe<sub>3</sub>O<sub>4</sub>/FWO composite semiconductor reached 91% after 30 min of dark adsorption and 60 min of catalytic reaction under photo-Fenton conditions. Compared with some other excellent photofenton catalysts (Table 1), 50%-Fe<sub>3</sub>O<sub>4</sub>/FWO also demonstrated better performance.

**Table 1.** Comparison of photocatalytic degradation of antibiotics.

Material	Dosage	Target	Concentration of Antibiotics	Knor ( $\text{min}^{-1} \text{mg}^{-1}$ )	Photocatalytic Degradation	Ref
50%-Fe <sub>3</sub> O <sub>4</sub> /FWO	25 mg	TCH	30 mg/L	0.0019	91%	This work
Fe/g-C <sub>3</sub> N <sub>4</sub> /kaolinite	25 mg	TC	20 ppm	0.0007	89%	[55]
TiO <sub>2</sub> -Cr	10 mg	amoxicillin	5 mg/L	0.0004	100%	[56]
Bi <sub>0.05</sub> La <sub>0.95</sub> FeO <sub>3</sub>	100 mg	TC	40 ppm	0.0003	79.57%	[57]
Bi <sub>2</sub> MoO <sub>6</sub> /NiFe LDH	50 mg	TC	10 mg/L	0.0004	95%	[58]
nitrogen-deficient and boron-doped g-C <sub>3</sub> N <sub>4</sub> nanotube (BCNNT)	50 mg	TC	20 mg/L	0.0011	80%	[59]
15%-AgBr-CaCO <sub>3</sub>	20 mg	TC	20 mg/L	0.0003	85%	[60]
ZnO/NiO/gC <sub>3</sub> N <sub>4</sub>	40 mg	TC	30 ppm	0.0013	91.49%	[61]

#### 2.4. Stability and Recyclability of Catalysts

Figure 7 illustrates the degradation curves of TCH in recycling experiments under the same experimental conditions. As shown, after three cycles, the degradation efficiency of TCH by the catalyst decreased to 74%. This decrease in efficiency could be attributed to two factors. Firstly, during the recovery process, the catalyst might not have been thoroughly washed, leading to a significant amount of pollutants adsorbed on the catalyst's surface, which blocked the active sites and thus reduced the degradation efficiency. Secondly, the stability of the catalyst might be relatively weak, resulting in a partial loss of catalytic activity and consequently fewer strong oxidative-free radicals generated during the recycling experiments, which affected the degradation efficiency of tetracycline hydrochloride. Additionally, since Fe<sub>3</sub>O<sub>4</sub> is strongly magnetic and FeWO<sub>4</sub> is non-magnetic, there might be certain difficulties in the recovery process. Therefore, it is necessary to assess whether the composite catalyst retains its magnetic properties after compounding.

Figure 8 shows the images of the catalyst being absorbed by magnets after being shaken in aqueous solution. It can be seen from Figure 8a that FeWO<sub>4</sub> was not absorbed by magnets in the turbidity state, indicating that FeWO<sub>4</sub> cannot be magnetically separated during the recovery of the catalyst. Figure 8b is a picture of the composite catalyst absorbed by the magnet without the degradation experiment. It can be seen that the composite catalyst has strong magnetism and can be completely absorbed by the magnet without producing turbidity. Figure 8c,d are the remaining catalysts after one degradation experiment and three cycles of the experiment, respectively. It can be seen that the composite catalyst still has strong magnetic properties after the degradation experiment, and although it shows a weak turbidity, the catalyst can easily gather together under the attraction of magnets. This indicates that the catalyst prepared in this experiment can be easily recovered by magnetic separation technology in practical application, which will not affect the turbidity of water while reducing the cost of catalyst separation and recovery.

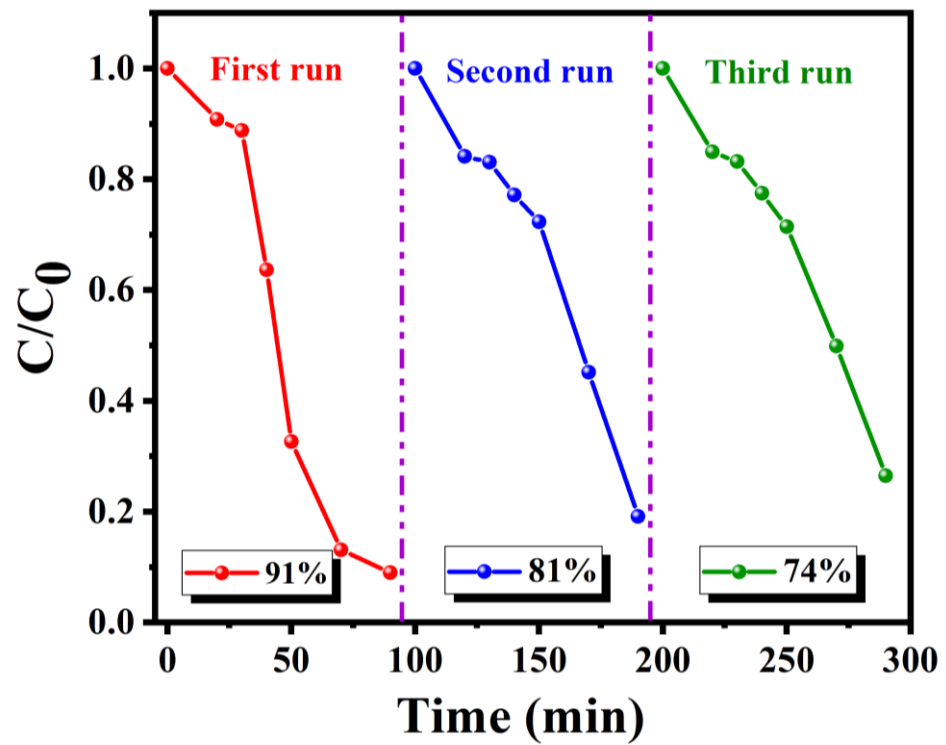


Figure 7. Recycle performance of 50%-Fe<sub>3</sub>O<sub>4</sub>/FWO.

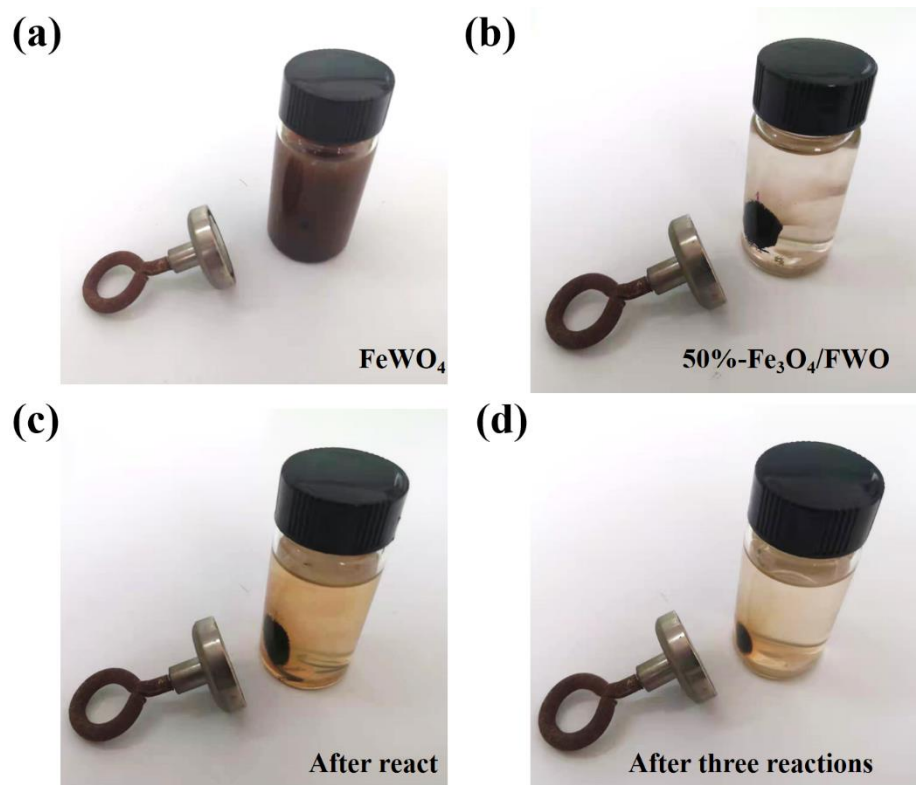
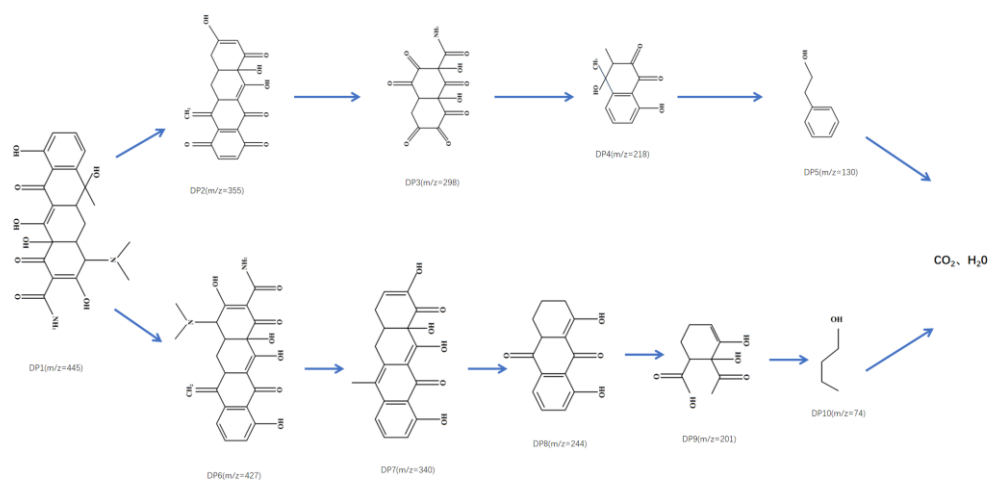


Figure 8. Magnetic test comparison of (a) FeWO<sub>4</sub>, (b) 50%-Fe<sub>3</sub>O<sub>4</sub>/FWO, (c) 50%-Fe<sub>3</sub>O<sub>4</sub>/FWO after react and (d) 50%-Fe<sub>3</sub>O<sub>4</sub>/FWO after three reactions.

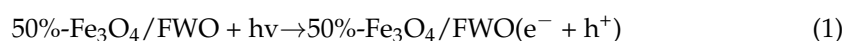
## 2.5. Mechanism Analysis

The degradation intermediates of TCH during the reaction were identified through LC-MS, proposing two main degradation pathways. As illustrated in Figure 9, Pathway 1 involves the formation of DP1 ( $m/z = 445$ ) from TCH, followed by the elimination of amino, ketone and hydroxyl groups to form DP2 ( $m/z = 355$ ). This intermediate then undergoes ring-opening, demethylation and amino group incorporation to form DP3 ( $m/z = 298$ ). Subsequent reactions lead to the formation of DP4 ( $m/z = 218$ ) and DP5 ( $m/z = 130$ ). In Pathway 2, TCH first undergoes hydroxyl group alteration to form a carbon-carbon double bond, resulting in DP6 ( $m/z = 427$ ). This intermediate then undergoes deamination and ketone removal to form DP7 ( $m/z = 340$ ), followed by ring-opening and deketonization reactions to yield DP8 ( $m/z = 244$ ) and DP9 ( $m/z = 201$ ). Ultimately, through the combined actions of both pathways, TCH is converted to  $H_2O$  and  $CO_2$  [62,63].



**Figure 9.** Possible degradation products and pathways of TCH.

Based on the Mott-Schottky tests and the calculation of the band gap, the conduction band (CB) and valence band (VB) positions of  $Fe_3O_4$  are  $E_{CB} = -0.7$  eV and  $E_{VB} = 1.5$  eV, respectively, while those of  $FeWO_4$  are  $E_{CB} = -0.3$  eV and  $E_{VB} = 2.2$  eV, respectively. Thus, the degradation mechanism diagram illustrated in Figure 10 was drawn. In this diagram,  $FeWO_4$  is a p-type semiconductor, and  $Fe_3O_4$  is an n-type semiconductor. Upon forming a composite, they create a p-n heterojunction. In this experiment, the photo-Fenton degradation of tetracycline hydrochloride begins with the generation of  $e^-$  and  $h^+$  in the photocatalyst under visible light irradiation (Equation (1)). The electrons transition from the VB to the CB of both  $Fe_3O_4$  and  $FeWO_4$ , leaving positively charged holes in the VB. Due to the presence of the p-n heterojunction, the electrons migrate from the CB of  $Fe_3O_4$  to the CB of  $FeWO_4$ , delaying the recombination of electron hole pairs. The electrons that remain in the CB of  $FeWO_4$  are partly captured by  $O_2$ , forming superoxide radicals ( $\cdot O_2^-$ ) that participate in the degradation reaction (Equation (2)). Another portion of the electrons is captured by Fe(III), which undergoes reduction to form Fe(II), thereby accelerating the degradation reaction (Equation (3)). Simultaneously, the holes in the CB of  $FeWO_4$  transfer to the VB of  $Fe_3O_4$ , further preventing the recombination of photogenerated electron hole pairs and enhancing the generation of reactive species. In the presence of hydrogen peroxide, Fe(II) in the semiconductor catalyzes the formation of hydroxyl radicals ( $\cdot OH$ ) from  $H_2O_2$ , which are involved in the catalytic process (Equation (4)). Finally,  $\cdot O_2^-$  and  $\cdot OH$  together break down the structure of tetracycline hydrochloride into  $H_2O$  and  $CO_2$  (Equation (5)).



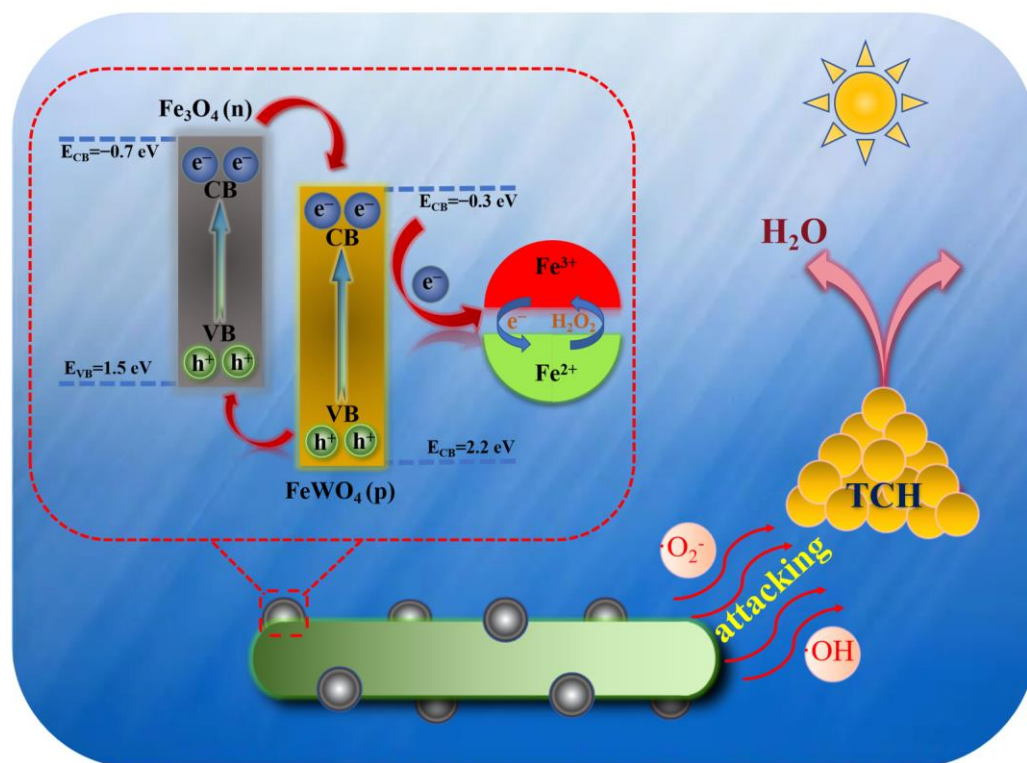


**Figure 10.** Possible mechanism of degradation of TCH in the 50%-Fe<sub>3</sub>O<sub>4</sub>/FWO photo-Fenton system.

### 3. Materials and Methods

#### 3.1. Materials

Sodium tungstate (Na<sub>2</sub>WO<sub>4</sub>•2H<sub>2</sub>O, Sinopod Group Chemical Reagent Co., Ltd., Shanghai, China), sodium hydroxide (NaOH, Sinopod Group Chemical Reagent Co., Ltd., Shanghai, China), sodium acetate (CHCOONa, Sinopod Group Chemical Reagent Co., Ltd., Shanghai, China), ferric chloride (FeCl<sub>3</sub>•6H<sub>2</sub>O, Sinopod Group Chemical Reagent Co., Ltd., Shanghai, China), tetracycline hydrochloride (CHClN<sub>2</sub>O<sub>8</sub>, Sinopod Group Chemical Reagent Co., Ltd., Shanghai, China). Ammonium ferrous sulfate (Fe(NH<sub>4</sub>)<sub>2</sub>•(SO<sub>4</sub>)<sub>2</sub>•6H<sub>2</sub>O, Tianjin Damao Chemical reagent Factory, Tianjin, China). Anhydrous ethanol (C<sub>2</sub>H<sub>6</sub>O, Tianjin Fuyu Fine Chemical Co., Ltd., Tianjin, China) and glycol ((CH<sub>2</sub>OH)<sub>2</sub>, Tianjin Fuyu Fine Chemical Co., Ltd., Tianjin, China). None of the drugs used was purified further.

#### 3.2. Catalyst Synthesis

##### 3.2.1. Preparation of Fe<sub>3</sub>O<sub>4</sub>

Referring to the previous study, we synthesized Fe<sub>3</sub>O<sub>4</sub> by a simple hydrothermal method [64]. A certain amount of sodium acetate was dissolved in 30 mL of ethylene glycol and stirred uniformly in a constant temperature magnetic stirrer. Then a certain amount of ferric chloride was dissolved in the above solution and continued to stir for 20–30 min until the mixture was completely mixed. After the stirring, the mixture was poured into 50 mL of polytetrafluoroethylene lining and hydrothermally treated at 180 °C for 12 h. After the reaction, it was washed three times with ultrapure water and anhydrous ethanol, and finally dried in an oven at 60 °C for 12 h.



### 3.2.2. Preparation of FeWO<sub>4</sub> Nanomaterials

For the preparation of FeWO<sub>4</sub>, we referred to the relevant steps in the published article [65], and made adjustments for the situation at hand to achieve the best effect: we dissolved 3 mmol Fe(NH<sub>4</sub>)<sub>2</sub>•(SO<sub>4</sub>)<sub>2</sub>•6H<sub>2</sub>O and 3 mmol Na<sub>2</sub>WO<sub>4</sub>•2H<sub>2</sub>O in 50 mL ultra-pure water, stirred magnetically for 30 min until completely dissolved, then added 2 M NaOH drop by drop while stirring until the pH reached about 8, and then stirred for 30 min. After the stirring, the homogeneous solution was placed in a hydrothermal reactor of 100 mL polytetrafluoroethylene inner tank, and the hydrothermal reaction was conducted at 180 °C for 12 h. When the reaction was complete, we washed the samples three times each with deionized water and anhydrous ethanol. Then they were dried in an oven at 60 °C for 12 h, and finally ground and collected to obtain FeWO<sub>4</sub> nanomaterial, labeled FWO.

### 3.2.3. Preparation of Fe<sub>3</sub>O<sub>4</sub>-FeWO<sub>4</sub> Composite Catalyst

The synthetic steps of Fe<sub>3</sub>O<sub>4</sub>-FeWO<sub>4</sub> composite samples were similar to those for Fe<sub>3</sub>O<sub>4</sub>, except different amounts of FeWO<sub>4</sub> were added during the synthesis process. The specific steps were as follows: A certain amount of sodium acetate was dissolved in 20 mL of ethylene glycol, and a certain amount of ferric chloride was slowly added to form a uniform mixed solution under stirring. A total of 1 mmol of ferrous tungstate powder was dissolved in 10 mL of ethylene glycol and ultrasonically dispersed for 5 min. Then it was added to the above mixed solution and stirred for 30 min. After stirring, the mixed solution was transferred to 50 mL of polytetrafluoroethylene lining for the hydrothermal reaction at 180 °C for 12 h. After the reaction, it was washed three times with anhydrous ethanol and ultrapure water to remove impurities. Finally, it was dried in an oven at 60 °C overnight to obtain x-Fe<sub>3</sub>O<sub>4</sub>.

### 3.3. Characterization

The morphology, structure and optical properties of the materials were characterized by X-ray powder diffraction (XRD, X 'PertPRO type, PANalytical B.V., Alemlo, Netherlands), BET (ASAP 2460 3.01 type, Thermo Fisher Scientific, Shanghai, China), FT-IR (DTGS KBr type Thermo Fisher Scientific, Shanghai, China), X-ray photoelectron spectroscopy (XPS, K-Alpha type, Thermo Fisher Scientific, Shanghai, China), UV-vis diffuse reflectance spectroscopy (UV-vis, Agilent Cary 100 type, Santa Clara, CA, USA), scanning electron microscopy (SEM, Zeiss Sigma 300 type, Oberkochen, Germany) and X-ray energy dispersive spectroscopy (EDS, Zeiss Sigma 300 type, Oberkochen, Germany). The CHI760E electrochemical workstation (Austin, TX, USA) was used to carry out the Mott-Schottky test to determine the type of semiconductor, current density and flat band potential; combined with the UV-vis DRS test, the conduction band position and valence band position could be calculated.

### 3.4. Evaluation of Solar Light Irradiation Photocatalytic Activities

The photo-Fenton degradation experiment was carried out in CEL-LAB500E4 photochemical reaction apparatus with TCH as the target pollutant. Specific operation steps were: 25 mg of catalyst was dispersed into a quartz reaction tube containing 40 mL of TCH solution of different concentrations. The photocatalyst degradation apparatus was continuously stirred for 30 min under dark conditions to achieve adsorption-desorption equilibrium. Then, a certain amount of H<sub>2</sub>O<sub>2</sub> was added to the solution and a 300 W xenon lamp with a 420 nm filter was turned on to trigger the photofenton reaction. Subsequently, 3 mL suspension was taken at regular intervals and filtered through a millipore filter with a pore size of 0.22 μm. Finally, the absorbance of the solution at 357 nm was measured by UV-vis spectrophotometer. The photo-Fenton degradation efficiency Y was obtained from Equation (6), and the first-order kinetic constant k of the reaction was obtained from Equation (7), where C<sub>0</sub> and C are the initial and measured concentrations of TCH solution, respectively. To test the reusable performance of the composite photocatalyst, the reaction solution was first centrifuged and collected, then washed three times with deionized water

and dried at 60 °C for 12 h to obtain the material for the next degradation. In order to test the magnetic recyclability of the catalyst, we added the catalyst to a glass vial filled with water and shook it, tested its magnetism with a magnet and took a physical picture. To further characterize the activity of the catalyst, we calculated the normalized rate constant  $k_{\text{nor}}$  [66]. The normalized rate constant was calculated using the formula  $k_{\text{nor}} = k_{\text{app}}/m$ , where  $k_{\text{app}}$  is the apparent reaction rate constant, which is the same as the aforementioned  $k$ , and  $m$  is the mass of the catalyst. This parameter helps to more accurately represent the activity of the catalyst per unit mass, thereby enhancing the comparability of results under different research conditions.

$$Y = (1 - C/C_0) \times 100\% \quad (6)$$

$$kt = \ln (C_0/C) \quad (7)$$

#### 4. Conclusions

In this experiment, a photocatalyst with a p-n heterojunction structure, 50%-Fe<sub>3</sub>O<sub>4</sub>/FWO, was successfully prepared. Under visible light conditions, various single-factor effect experiments were conducted to optimize the degradation conditions. The optimal conditions were determined to be an initial pollutant concentration of 30 mg/L, an initial solution pH of 4, a catalyst dosage of 25 mg and an addition of 30 µL of H<sub>2</sub>O<sub>2</sub>. Under these conditions, the degradation efficiency of TCH reached 91% within 60 min, which is a significant improvement compared to the individual semiconductors Fe<sub>3</sub>O<sub>4</sub> and FeWO<sub>4</sub>. Photochemical test results showed that the composite catalyst had superior photoelectrochemical response density and impedance compared to the individual catalysts, indicating a faster electron transfer rate and higher electron hole separation efficiency. The degradation mechanism analysis demonstrated that the presence of the p-n heterojunction greatly increased the electron migration rate, delayed the recombination time of photogenerated electron hole pairs and enhanced the Fe(II)/Fe(III) cycling rate in the heterogeneous photo-Fenton process, thus improving the degradation efficiency. Furthermore, the magnetic properties of the composite catalyst were compared, and it was found that even after three degradation experiments, the catalyst still retained strong magnetism. This study indicates that the composite catalyst 50%-Fe<sub>3</sub>O<sub>4</sub>/FWO not only possesses high photo-Fenton degradation efficiency but also maintains magnetism, facilitating sample recovery and reuse. These findings provide a potential approach for the practical application of the photo-Fenton method.

**Author Contributions:** B.B.: Conceptualization, Writing—Original Draft, Writing—Review and Editing, Investigation; G.C.: Visualization; X.C.: Formal analysis; J.C.: Data curation; X.C.: Methodology; Q.W.: Supervision, Project administration, Resources. All authors have read and agreed to the published version of the manuscript.

**Funding:** This work was financially supported by the Innovative Research Team for Science and Technology of Shaanxi Province (2022TD-04) and Jiangxi Provincial Department of Science and Technology (20212BCJ23031).

**Data Availability Statement:** Data are contained within the article.

**Conflicts of Interest:** The authors declare no conflicts of interest.

#### References

1. Wang, J.; Zhuan, R. Degradation of antibiotics by advanced oxidation processes: An overview. *Sci. Total Environ.* **2020**, *701*, 135023. [[CrossRef](#)]
2. Danner, M.-C.; Robertson, A.; Behrends, V.; Reiss, J. Antibiotic pollution in surface fresh waters: Occurrence and effects. *Sci. Total Environ.* **2019**, *664*, 793–804. [[CrossRef](#)] [[PubMed](#)]
3. Kovalakova, P.; Cizmas, L.; McDonald, T.J.; Marsalek, B.; Feng, M.; Sharma, V.K. Occurrence and toxicity of antibiotics in the aquatic environment: A review. *Chemosphere* **2020**, *251*, 126351. [[CrossRef](#)] [[PubMed](#)]

4. Wang, M.; Wang, Y.; Li, Y.; Wang, C.; Kuang, S.; Ren, P.; Xie, B. Persulfate oxidation of tetracycline, antibiotic resistant bacteria, and resistance genes activated by Fe doped biochar catalysts: Synergy of radical and non-radical processes. *Chem. Eng. J.* **2023**, *464*, 142558. [[CrossRef](#)]
5. Yu, Y.; Jin, Q.; Ren, Y.; Wang, Y.; Zhu, D.; Wang, J. Ratiometric fluorescent sensor based on europium (III)-functionalized covalent organic framework for selective and sensitive detection of tetracycline. *Chem. Eng. J.* **2023**, *465*, 142819. [[CrossRef](#)]
6. Zhao, H.; Wang, Z.; Liang, Y.; Wu, T.; Chen, Y.; Yan, J.; Zhu, Y.; Ding, D. Adsorptive decontamination of antibiotics from livestock wastewater by using alkaline-modified biochar. *Environ. Res.* **2023**, *226*, 115676. [[CrossRef](#)]
7. Nian, Q.; Yang, H.; Meng, E.; Wang, C.; Xu, Q.; Zhang, Q. Efficient adsorptive removal of aminoglycoside antibiotics from environmental water. *Chemosphere* **2023**, *337*, 139379. [[CrossRef](#)] [[PubMed](#)]
8. Zou, M.; Tian, W.; Chu, M.; Lu, Z.; Liu, B.; Xu, D. Magnetically separable laccase-biochar composite enable highly efficient adsorption-degradation of quinolone antibiotics: Immobilization, removal performance and mechanisms. *Sci. Total Environ.* **2023**, *879*, 163057. [[CrossRef](#)]
9. Wang, C.; Lin, C.-Y.; Liao, G.-Y. Degradation of antibiotic tetracycline by ultrafine-bubble ozonation process. *J. Water Process Eng.* **2020**, *37*, 101463. [[CrossRef](#)]
10. Adamek, E.; Baran, W. Degradation of veterinary antibiotics by the ozonation process: Product identification and ecotoxicity assessment. *J. Hazard. Mater.* **2024**, *469*, 134026. [[CrossRef](#)]
11. Wu, F.; Yuan, C.; Ruan, C.; Zheng, M.; Liu, L.; Wang, G.; Chen, G. Coagulation promotes the spread of antibiotic resistance genes in secondary effluents. *Environ. Pollut.* **2024**, *355*, 124245. [[CrossRef](#)] [[PubMed](#)]
12. Dong, Y.; Zhang, J.; Wang, Q.; Xu, D.; Pang, S.; Campos, L.C.; Ren, Z.; Wang, P. Dual function of magnetic field in enhancing antibiotic wastewater treatment by an integrated photocatalysis and fluidized bed biofilm reactor (FBBR). *J. Environ. Manag.* **2023**, *347*, 119249. [[CrossRef](#)] [[PubMed](#)]
13. Cheng, D.; Ngo, H.H.; Guo, W.; Chang, S.W.; Nguyen, D.D.; Liu, Y.; Shan, X.; Nghiem, L.D.; Nguyen, L.N. Removal process of antibiotics during anaerobic treatment of swine wastewater. *Bioresour. Technol.* **2020**, *300*, 122707. [[CrossRef](#)] [[PubMed](#)]
14. Qin, G.; Song, X.; Chen, Q.; He, W.; Yang, J.; Li, Y.; Zhang, Y.; Wang, J.; Dionysiou, D.D. Novel durable and recyclable Cu@MoS<sub>2</sub>/polyacrylamide/copper alginate hydrogel photo-Fenton-like catalyst with enhanced and self-regenerable adsorption and degradation of high concentration tetracycline. *Appl. Catal. B Environ. Energy* **2024**, *344*, 123640. [[CrossRef](#)]
15. Zhang, X.; Gu, W.; Liu, D.; Zhou, L.; Huy, N.N.; Wang, L.; Zhang, J.; Liu, Y.; Lei, J. Fe(II) and Pyridinic N complex sites synergy to activate PMS for specific generation of 1O<sub>2</sub> to degrade antibiotics with high efficiency. *Sci. Total Environ.* **2023**, *892*, 164067. [[CrossRef](#)] [[PubMed](#)]
16. Yi, J.; Abdullah Al-Dhabi, N.; Hu, T.; Soyol-Erdene, T.-O.; Bayanjargal, O.; Liu, E.; Tang, W. Highly efficient degradation of antibiotic metronidazole by an environmental-friendly metal-free dual-cathode electro-Fenton system. *Chem. Eng. J.* **2024**, *492*, 152447. [[CrossRef](#)]
17. Wu, X.; Chen, G.; Li, L.; Wang, J.; Wang, G. ZnIn<sub>2</sub>S<sub>4</sub>-based S-scheme heterojunction photocatalyst. *J. Mater. Sci. Technol.* **2023**, *167*, 184–204. [[CrossRef](#)]
18. Zhang, Y.; Liu, H.; Gao, F.; Tan, X.; Cai, Y.; Hu, B.; Huang, Q.; Fang, M.; Wang, X. Application of MOFs and COFs for photocatalysis in CO<sub>2</sub> reduction, H<sub>2</sub> generation, and environmental treatment. *EnergyChem* **2022**, *4*, 100078. [[CrossRef](#)]
19. Ge, X.; Meng, G.; Liu, B. Efficient degradation of antibiotics by oxygen vacancy-LaFeO<sub>3</sub>/polystyrene-driven photo-Fenton system: Highlight the impacts of molecular structures. *J. Water Process Eng.* **2023**, *51*, 103428. [[CrossRef](#)]
20. Hou, D.; Luo, J.; Sun, Q.; Zhang, M.; Wang, J. Preparation of Co-CNK-OH and Its Performance in Fenton-like Photocatalytic Degradation of Tetracycline. *Catalysts* **2023**, *13*, 715. [[CrossRef](#)]
21. Li, J.; Li, Y.; Chen, M.; Tang, X.; Zhu, N.; Li, W.; Mei, Q.; Yue, S.; Tang, Y.; Wang, Q. Construction of polynary systems by coupling Cd/CdS with magnetic recyclable CuO/Fe<sub>2</sub>O<sub>3</sub>/CuFe<sub>2</sub>O<sub>4</sub> nanocomposite for enhancing photo-Fenton degradation of antibiotics. *J. Environ. Chem. Eng.* **2023**, *11*, 111089. [[CrossRef](#)]
22. Dai, H.; Liu, Z.; Ou, L.; Shen, Y.; Ning, Z.; Hu, F.; Peng, X. Iron nanoparticles decorated TiO<sub>2</sub> hollow microspheres for boosting degradation of tetracycline in a photo-Fenton catalytic system. *J. Environ. Chem. Eng.* **2023**, *11*, 110797. [[CrossRef](#)]
23. Chu, Y.; Liu, C.; Wang, R.; Chen, H. Development of heterogenous electro-Fenton process with immobilized FeWO<sub>4</sub> catalyst for the degradation of tetracycline and the treatment of crude oil tank cleaning wastewater in neutral medium. *Chem. Eng. J.* **2023**, *465*, 142964. [[CrossRef](#)]
24. Xu, L.; Wu, X.-Q.; Li, C.-Y.; Liu, N.-P.; An, H.-L.; Ju, W.-T.; Lu, W.; Liu, B.; Wang, X.-F.; Wang, Y.; et al. Sonocatalytic degradation of tetracycline by BiOBr/FeWO<sub>4</sub> nanomaterials and enhancement of sonocatalytic effect. *J. Clean. Prod.* **2023**, *394*, 136275. [[CrossRef](#)]
25. Li, Y.; Wang, Q.; Zhang, X.; Dong, L.; Zhang, M.; Rao, P.; Gao, N.; Sun, Y.; Deng, J. Development of a heterogenous catalyst FeWO<sub>4</sub>/Cu<sub>2</sub>S as peroxymonosulfate activator for effective sulfachloropyridazine elimination. *J. Clean. Prod.* **2024**, *434*, 140098. [[CrossRef](#)]
26. Liu, J.; Liu, Q.; Li, J.; Zheng, X.; Liu, Z.; Guan, X. Photochemical conversion of oxalic acid on heterojunction engineered FeWO<sub>4</sub>/g-C<sub>3</sub>N<sub>4</sub> photocatalyst for high-efficient synchronous removal of organic and heavy metal pollutants. *J. Clean. Prod.* **2022**, *363*, 132527. [[CrossRef](#)]
27. Wu, J.-C.; Shen, X.-C.; Wang, H.; Deng, D.-J.; Wu, S.-Q.; Gong, Y.; Zhu, L.-H.; Xu, L.; Li, H.-N. Electronic structure modification of FeWO<sub>4</sub> through F doping for enhanced oxygen reduction performance in zinc-air batteries. *Mater. Today Phys.* **2023**, *38*, 101274. [[CrossRef](#)]

28. Wang, J.; Wang, M.; Kang, J.; Tang, Y.; Liu, J.; Li, S.; Xu, Z.; Tang, P. The promoted tetracycline visible-light-driven photocatalytic degradation efficiency of g-C<sub>3</sub>N<sub>4</sub>/FeWO<sub>4</sub> Z-scheme heterojunction with peroxymonosulfate assisting and mechanism. *Sep. Purif. Technol.* **2022**, *296*, 121440. [[CrossRef](#)]
29. Xu, H.-Y.; Wang, W.-S.; Li, B.; Zhang, L. Mechanism insights into the enhanced photocatalytic peroxydisulfate activation by Fe<sub>3</sub>O<sub>4</sub>/BiOI heterojunction. *Mater. Sci. Eng. B* **2023**, *294*, 116509. [[CrossRef](#)]
30. Shekofteh-Gohari, M.; Habibi-Yangjeh, A. Combination of CoWO<sub>4</sub> and Ag<sub>3</sub>VO<sub>4</sub> with Fe<sub>3</sub>O<sub>4</sub>/ZnO nanocomposites: Magnetic photocatalysts with enhanced activity through p-n-n heterojunctions under visible light. *Solid State Sci.* **2017**, *74*, 24–36. [[CrossRef](#)]
31. Dang, J.; Guo, J.; Wang, L.; Guo, F.; Shi, W.; Li, Y.; Guan, W. Construction of Z-scheme Fe<sub>3</sub>O<sub>4</sub>/BiOCl/BiOI heterojunction with superior recyclability for improved photocatalytic activity towards tetracycline degradation. *J. Alloys Compd.* **2022**, *893*, 162251. [[CrossRef](#)]
32. Sun, H.; Wang, L.; Wang, X.; Dong, Y.; Pei, T. A magnetically recyclable Fe<sub>3</sub>O<sub>4</sub>/ZnIn<sub>2</sub>S<sub>4</sub> type-II heterojunction to boost photocatalytic degradation of gemifloxacin. *Appl. Surf. Sci.* **2024**, *656*, 159674. [[CrossRef](#)]
33. Xiao, M.; Li, R.; Hu, X.; Zhu, W.; Yu, Z.; Xiao, H.; Wang, W.; Yang, T. Construction of in-situ carbon-doped TiO<sub>2</sub> decorated Fe<sub>3</sub>O<sub>4</sub> heterojunction and their enhanced photocatalytic oxidation of As(III) under visible light. *Sep. Purif. Technol.* **2022**, *300*, 121836. [[CrossRef](#)]
34. Li, S.; Wang, Z.; Zhang, X.; Zhao, J.; Hu, Z.; Wang, Z.; Xie, X. Preparation of magnetic nanosphere/nanorod/nanosheet-like Fe<sub>3</sub>O<sub>4</sub>/Bi<sub>2</sub>S<sub>3</sub>/BiOBr with enhanced (0 0 1) and (1 1 0) facets to photodegrade diclofenac and ibuprofen under visible LED light irradiation. *Chem. Eng. J.* **2019**, *378*, 122169. [[CrossRef](#)]
35. Thabet, M.; Abd El-Monaem, E.M.; Alharbi, W.R.; Mohamoud, M.; Abdel-Aty, A.-H.; Ibrahim, I.; Abdel-Lateef, M.A.; Goda, A.E.S.; Seaf Elnasr, T.A.; Wang, R.; et al. Adsorption and photocatalytic degradation activities of a hybrid magnetic mesoporous composite of α-Fe<sub>2</sub>O<sub>3</sub> nanoparticles embedded with sheets-like MgO. *J. Water Process Eng.* **2024**, *60*, 105192. [[CrossRef](#)]
36. Zebiri, Z.; Debbache, N.; Sehili, T. Sheet-like g-C<sub>3</sub>N<sub>4</sub> for enhanced photocatalytic degradation of naproxen. *J. Photochem. Photobiol. A Chem.* **2024**, *446*, 115189. [[CrossRef](#)]
37. Wang, X.; Liu, F.; Liang, W.; Zhang, W. Characterization of Electromagnetic Catalysis and Degradation of Allogenic Odor Using Fe<sub>3</sub>O<sub>4</sub> Nanoparticles with Tannin Coating. *ACS EST Eng.* **2021**, *1*, 1542–1552. [[CrossRef](#)]
38. Bojabady, F.; Kamali-Heidari, E.; Sahebani, S. Hydrothermal synthesis of highly aligned Fe<sub>3</sub>O<sub>4</sub> nanoslates on nickel foam. *Mater. Chem. Phys.* **2023**, *305*, 127828. [[CrossRef](#)]
39. Ali, M.D.; Aslam, A.; Haider, M.A.; Aftab, Z.e.H.; Fakhar, U.; ud-Din, S.Z.; Ezzine, S.; Ben Farhat, L.; Somaily, H.H. I-V, dielectric, antibacterial, and robust EMI shielding effectiveness properties of graphene/Fe<sub>3</sub>O<sub>4</sub>. *Inorg. Chem. Commun.* **2022**, *146*, 110039. [[CrossRef](#)]
40. Chakraborty, A.K.; Akter, S.; Ganguli, S.; Haque, M.A.; Nur, A.S.M.; Sabur, M.A. Design of FeWO<sub>4</sub>@N-TiO<sub>2</sub> nanocomposite and its enhanced photocatalytic activity in decomposing methylene blue and phenol under visible light. *Environ. Technol. Innov.* **2024**, *33*, 103536. [[CrossRef](#)]
41. Yang, Y.; Logesh, K.; Mehrez, S.; Huynen, I.; Elbadawy, I.; Mohanavel, V.; Alamri, S. Rational construction of wideband electromagnetic wave absorber using hybrid FeWO<sub>4</sub>-based nanocomposite structures and tested by the free-space method. *Ceram. Int.* **2023**, *49*, 2130–2139. [[CrossRef](#)]
42. Hafizi, H.; Lutfur Rahman, M.; Sani Sarjadi, M.; Salim Akhter, M.; Collins, M.N.; O'Reilly, E.J.; Walker, G.M.; Sarkar, S.M. Magnetically recyclable Schiff-based palladium nanocatalyst [Fe<sub>3</sub>O<sub>4</sub>@SiNSB-Pd] and its catalytic applications in Heck reaction. *Arab. J. Chem.* **2022**, *15*, 103914. [[CrossRef](#)]
43. Boily, J.-F.; Felmy, A.R. On the protonation of oxo- and hydroxo-groups of the goethite (α-FeOOH) surface: A FTIR spectroscopic investigation of surface O–H stretching vibrations. *Geochim. Et Cosmochim. Acta* **2008**, *72*, 3338–3357. [[CrossRef](#)]
44. Li, J.; Li, S.; Cao, Z.; Zhao, Y.; Wang, Q.; Cheng, H. Heterostructure CoFe<sub>2</sub>O<sub>4</sub>/kaolinite composite for efficient degradation of tetracycline hydrochloride through synergetic photo-Fenton reaction. *Appl. Clay Sci.* **2023**, *244*, 107102. [[CrossRef](#)]
45. Fan, G.; Cai, C.; Yang, S.; Du, B.; Luo, J.; Chen, Y.; Lin, X.; Li, X.; Wang, Y. Sonophotocatalytic degradation of ciprofloxacin by Bi<sub>2</sub>MoO<sub>6</sub>/FeVO<sub>4</sub> heterojunction: Insights into performance, mechanism and pathway. *Sep. Purif. Technol.* **2022**, *303*, 122251. [[CrossRef](#)]
46. Dong, Y.B.; Lin, H. Ammonia nitrogen removal from aqueous solution using zeolite modified by microwave-sodium acetate. *J. Cent. South Univ.* **2016**, *23*, 1345–1352. [[CrossRef](#)]
47. Ain, Q.U.; Rasheed, U.; Yaseen, M.; Zhang, H.; Tong, Z. Superior dye degradation and adsorption capability of polydopamine modified Fe<sub>3</sub>O<sub>4</sub>-pillared bentonite composite. *J. Hazard. Mater.* **2020**, *397*, 122758. [[CrossRef](#)]
48. Guo, H.; Jiang, N.; Wang, H.; Lu, N.; Shang, K.; Li, J.; Wu, Y. Degradation of antibiotic chloramphenicol in water by pulsed discharge plasma combined with TiO<sub>2</sub>/WO<sub>3</sub> composites: Mechanism and degradation pathway. *J. Hazard. Mater.* **2019**, *371*, 666–676. [[CrossRef](#)] [[PubMed](#)]
49. Hong, P.; Li, Y.; He, J.; Saeed, A.; Zhang, K.; Wang, C.; Kong, L.; Liu, J. Rapid degradation of aqueous doxycycline by surface CoFe<sub>2</sub>O<sub>4</sub>/H<sub>2</sub>O<sub>2</sub> system: Behaviors, mechanisms, pathways and DFT calculation. *Appl. Surf. Sci.* **2020**, *526*, 146557. [[CrossRef](#)]
50. Liu, Z.; Cui, E.; Wang, X.; Jin, Z. Energy band engineering over phosphorus-doped CdS/graphdiyne S-scheme heterojunction for enhance photocatalytic hydrogen production. *Chem. Eng. J.* **2024**, *486*, 150060. [[CrossRef](#)]
51. Narewadikar, N.A.; Pedanekar, R.S.; Parale, V.G.; Park, H.H.; Rajpure, K.Y. Spray deposited yttrium incorporated TiO<sub>2</sub> photoelectrode for efficient photoelectrocatalytic degradation of organic pollutants. *J. Rare Earths* **2023**, *41*, 1929–1937. [[CrossRef](#)]



52. Cao, Y.; Yuan, X.; Chen, H.; Wang, H.; Chen, Y.; Chen, J.; Huang, H.; Mou, Y.; Shangguan, Z.; Li, X. Rapid concurrent photocatalysis-persulfate activation for ciprofloxacin degradation by Bi<sub>2</sub>S<sub>3</sub> quantum dots-decorated MIL-53(Fe) composites. *Chem. Eng. J.* **2023**, *456*, 140971. [[CrossRef](#)]
53. Mahrsi, M.I.; Chouchene, B.; Gries, T.; Carré, V.; Medjahdi, G.; Ayari, F.; Balan, L.; Schneider, R. 0D/1D CuO-Cu<sub>2</sub>O/ZnO p-n heterojunction with high photocatalytic activity for the degradation of dyes and Naproxen. *J. Environ. Chem. Eng.* **2024**, *12*, 113072. [[CrossRef](#)]
54. Zhao, Y.; Cao, Z.; Chen, Y.; Jia, Y.; Wang, Q.; Cheng, H. Heterostructure coal-bearing strata kaolinite/MnFe<sub>2</sub>O<sub>4</sub> composite for activation of peroxydisulfate to efficiently degrade chlortetracycline hydrochloride. *Colloids Surf. A Physicochem. Eng. Asp.* **2022**, *643*, 128789. [[CrossRef](#)]
55. Cao, Z.; Jia, Y.; Wang, Q.; Cheng, H. High-efficiency photo-Fenton Fe/g-C<sub>3</sub>N<sub>4</sub>/kaolinite catalyst for tetracycline hydrochloride degradation. *Appl. Clay Sci.* **2021**, *212*, 106213. [[CrossRef](#)]
56. Wahyuni, E.T.; Cahyono, R.N.; Nora, M.; Alharissa, E.Z.; Kunarti, E.S. Degradation of amoxicillin residue under visible light over TiO<sub>2</sub> doped with Cr prepared from tannery wastewater. *Results Chem.* **2024**, *7*, 101302. [[CrossRef](#)]
57. James, A.; Rodney, J.D.; NK, U. Kinetic Comparison of Photocatalysis with the Photo-Fenton Process on the Removal of Tetracycline Using Bismuth-Modified Lanthanum Orthoferrite Nanostructures. *ACS Appl. Nano Mater.* **2024**, *7*, 11560–11574. [[CrossRef](#)]
58. Bharathi, A.M.; Mani, P.; Neppolian, B.; Soo, H.S.; Krishnamurthi, T. Fabrication of a Z-scheme Bi<sub>2</sub>MoO<sub>6</sub>/NiFe layered double hydroxide heterojunction for the visible light-driven degradation of tetracycline antibiotics. *J. Water Process Eng.* **2024**, *58*, 104813. [[CrossRef](#)]
59. Wen, S.; Tang, X.; Zhou, G.; Song, J.; Ma, R.; Mao, G.; Zhang, L.; Yin, J.; Ang, E.H. Gas-phase self-assembly: Converting 2D graphitic carbon nitride into 1D nanotubes for improved photocatalytic tetracycline degradation. *Ceram. Int.* **2024**, *50*, 14686–14696. [[CrossRef](#)]
60. Chen, Q.; Gao, M.; Yu, M.; Zhang, T.; Wang, J.; Bi, J.; Dong, F. Efficient photo-degradation of antibiotics by waste eggshells derived AgBr-CaCO<sub>3</sub> heterostructure under visible light. *Sep. Purif. Technol.* **2023**, *314*, 123573. [[CrossRef](#)]
61. Dineshbabu, N.; Jayaprakash, R.N.; Karuppasamy, P.; Arun, T.; Vijaya, J.J.; Nimshi, R.E.; Pandian, M.S.; Packiam, S.M.; Ramasamy, P. Investigation on Tetracycline degradation and bactericidal properties of binary and ternary ZnO/NiO/g-C<sub>3</sub>N<sub>4</sub> composites prepared by a facile co-precipitation method. *J. Environ. Chem. Eng.* **2022**, *10*, 107368. [[CrossRef](#)]
62. Zhang, Y.; Zhou, J.; Chen, X.; Wang, L.; Cai, W. Coupling of heterogeneous advanced oxidation processes and photocatalysis in efficient degradation of tetracycline hydrochloride by Fe-based MOFs: Synergistic effect and degradation pathway. *Chem. Eng. J.* **2019**, *369*, 745–757. [[CrossRef](#)]
63. Zheng, J.; Fan, C.; Li, X.; Yang, Q.; Wang, D.; Duan, A.; Ding, J.; Rong, S.; Chen, Z.; Luo, J.; et al. Enhanced photodegradation of tetracycline hydrochloride by hexameric AgBr/Zn-Al MMO S-scheme heterojunction photocatalysts: Low metal leaching, degradation mechanism and intermediates. *Chem. Eng. J.* **2022**, *446*, 137371. [[CrossRef](#)]
64. Ni, X.; Zhang, J.; Zhao, L.; Wang, F.; He, H.; Dramou, P. Study of the solvothermal method time variation effects on magnetic iron oxide nanoparticles (Fe<sub>3</sub>O<sub>4</sub>) features. *J. Phys. Chem. Solids* **2022**, *169*, 110855. [[CrossRef](#)]
65. Shi, X.; Wang, L.; Zuh, A.A.; Jia, Y.; Ding, F.; Cheng, H.; Wang, Q. Photo-Fenton reaction for the degradation of tetracycline hydrochloride using a FeWO<sub>4</sub>/BiOCl nanocomposite. *J. Alloys Compd.* **2022**, *903*, 163889. [[CrossRef](#)]
66. Qin, L.; Zeng, G.; Lai, C.; Huang, D.; Zhang, C.; Cheng, M.; Yi, H.; Liu, X.; Zhou, C.; Xiong, W.; et al. Synthetic strategies and application of gold-based nanocatalysts for nitroaromatics reduction. *Sci. Total Environ.* **2019**, *652*, 93–116. [[CrossRef](#)]

**Disclaimer/Publisher's Note:** The statements, opinions and data contained in all publications are solely those of the individual author(s) and contributor(s) and not of MDPI and/or the editor(s). MDPI and/or the editor(s) disclaim responsibility for any injury to people or property resulting from any ideas, methods, instructions or products referred to in the content.